RSC Advances

PAPER

View Article Online
View Journal | View Issue

Open Access Article. Published on 19 August 2021. Downloaded on 12/6/2025 5:40:57 AM.
This article is licensed under a Creative Commons Attribution-NonCommercial 3.0 Unported Licence.

Check for updates

Cite this: *RSC Adv.*, 2021, **11**, 28107

Freestanding symmetrical SiN/Si/SiN composite coated on carbon nanotube paper for a high-performance lithium-ion battery anode based on synergistic effects†

Xinyi He, ‡[a] Fan Yue,‡[a] Zhenzhen Shang,[a] Jian Wang,[a] Wenhua Gu*[b] and Xiaodong Huang *[a]

Received 15th June 2021
Accepted 6th August 2021

DOI: 10.1039/d1ra04630f

rsc.li/rsc-advances

Direct coating of Si on an elastic carbon nanotube (CNT) network effectively addresses the rapid capacity fading of the Si anode. However, this strategy is hindered by the low Si tap density (Si < 50 nm) since sufficient void space has to be left for accommodating the Si volume change. Also, the mechanical properties of the CNT network as the elastic buffer matrix degrade significantly caused by side reactions of CNT with electrolyte. This work presents a freestanding paper-like anode consisting of a symmetrical sandwich-structured SiN/Si/SiN composite grown on CNT paper. This anode works well (~259 μA h cm^{-2} under the current rate of 0.6C after 350 cycles, with a capacity retention of 73.8%) even when the CNT is filled by the composite without void space left for accommodating volume expansion. This is mainly due to the following synergistic effects: on one hand, the stress-compensation phenomenon in the symmetrical sandwich-structured composite balances the volume change-induced stress and thus the composite has a robust mechanical stability with an intact morphology during cycling. On the other hand, the intact composite avoids reaction of CNT with the electrolyte and thus the CNT retains excellent mechanical properties and serves well as the elastic buffer matrix. These two sides interact with each other, enabling the high anode performance.

1. Introduction

The rapid development of portable electronics in recent years has made an urgent demand on high-energy-density lithium-ion batteries (LIB) to enhance the battery life. To meet this demand, it is necessary to find an appropriate anode material to replace the traditional graphite (372 mA h g^{-1}). Due to its ultrahigh specific capacity (3579 mA h g^{-1} for $Li_{15}Si_4$), low discharge potential (≤0.4 V *versus* Li/Li^+) and cost effectiveness, Si has been regarded as a promising anode for improving the LIB energy density.[1–4] However, stress caused by the Si huge volume change (300% for $Li_{15}Si_4$) during the lithiation and delithiation processes would lead to cracks of the Si anode and thus poor cycling stability with rapid capacity fading. Extensive strategies have been investigated to overcome this issue mainly by engineering the anode composites (*e.g.* Si/C and Si/SiN) and nanostructures (*e.g.* Si nanowire, and nanotube).[3–40,53,54] As illustrated in Fig. 1(a), it is effective and facile to construct a nanostructured Si anode by direct deposition of Si on a carbon nanotube (CNT) network (denoted as Si/CNT), such as CNT sponge and CNT paper.[24–40] In these configurations, CNT serves not only as a conductive network (or current collector), but also as an elastic buffer matrix to accommodate the Si volume change. Moreover, compared with rigid metal current collectors (*e.g.* Cu and steel), CNTs are electrochemically active and lightweight;[41–43] Therefore, the Si/CNT configurations also help improve the overall specific capacity in terms of the whole anode volume or gravity (including the Si and current collector).[22,23,36–40] However, in order to reserve enough void space for accommodating the Si volume change, the Si content coated on the CNT frame (in the form of Si nanofilms or nanoparticles and their typical size < 50 nm) is usually quite low,[19–23,28–40] which results in a relatively low tap density and thus a low specific capacity since the Si component is the main contributor to the overall specific capacity in a Si/CNT anode (Si ~3579 mA h g^{-1} *vs.* CNT ~400 mA h g^{-1}).[2–4,34,41–43] Therefore, there is a trade-off between good cycling stability and high specific capacity for the current Si/CNT anode configurations as reported in the literature.[19–23,28–40]

This work mainly focuses on the above trade-off in the current Si/CNT anodes by rationally designing both the anode

[a]*Key Laboratory of MEMS of the Ministry of Education, Southeast University, Nanjing 210096, China. E-mail: xdhuang@seu.edu.cn*

[b]*School of Electronic and Optical Engineering, Nanjing University of Science and Technology, Nanjing 210094, China. E-mail: guwenhua@njust.edu.cn*

† Electronic supplementary information (ESI) available. See DOI: 10.1039/d1ra04630f

‡ X. H. and F. Y. contributed equally to this work.

Open Access Article. Published on 19 August 2021. Downloaded on 12/6/2025 5:40:57 AM.
This article is licensed under a Creative Commons Attribution-NonCommercial 3.0 Unported Licence.

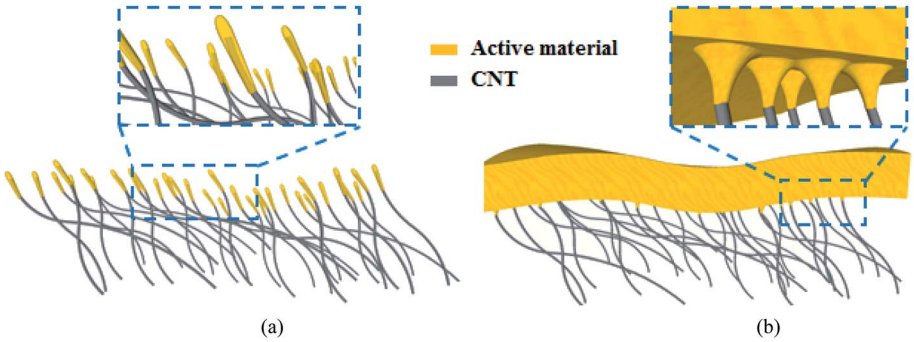

Fig. 1 (a) Schematic illustration of the conventional active film/CNT anode configuration. The film coated on the CNT network is thin enough (<50 nm) to enable sufficient void space left for accommodating the Si volume change during the lithiation and delithiation processes. (b) Schematic illustration of the proposed anode configuration in this work. The thickness of the active film increases to 500 nm and thus the void space of the CNT network is filled by the film. Unlike the conventional anode in (a) which relies on the void space to improve the mechanical stability, the proposed anode in (b) is based on the synergistic effects to achieve the robust mechanical stability.

composites (including Si, SiN and their composites) and structures (Si, SiN and their stacks). The anode with a symmetrical sandwich-structured SiN/Si/SiN composite coated on the CNT paper (denoted as NSN@CNT) displays high reversible specific capacity, good cycling stability and high rate performance even when the composite thickness is up to 500 nm and the void space of the CNT network is fully filled by the composite, as illustrated in Fig. 1(b). By systematically characterizing the electrochemical behaviors and microstructures of a series of anodes with different composites, structures and substrates (including CNT and stainless-steel substrates), it is revealed that the following synergistic effects are responsible for the high performance of the NSN@CNT anode: on one hand, the stress-compensation phenomenon involved in the symmetrical sandwich-structured SiN/Si/SiN composite can balance and suppress the volume change-induced stress and also the elastic CNT paper is helpful to release the stress. These cause that the SiN/Si/SiN composite maintains a strong mechanical stability with an intact morphology with cycling; on the other hand, the intact composite can effectively avoid reaction of the CNT with the electrolyte. Consequently, degradation of the CNT mechanical properties caused by reaction of CNT with the electrolyte is successfully prevented and alternatively the CNT network retains excellent mechanical properties with high elasticity and serves effectively as the elastic buffer matrix for stress relaxation. The above two sides interrelate and interact with each other. These synergistic effects enable that the NSN@CNT anode exhibits much better performance than its counterpart on the stainless steel substrate and other anodes with different composites, structures and substrates in this work.

2. Experimental

CNT paper (from XFNANO Corp.) and stainless steel (SS, from MTI Corp.) were used as the elastic and rigid substrates respectively. To prepare the symmetrical sandwich-structured SiN/Si/SiN composite, 125 nm SiN, 250 nm Si and 125 nm SiN were deposited sequentially on the substrates by plasma-enhanced chemical vapor deposition with NH_3/SiH_4 (13.5 sccm/13.5 sccm) as the precursor for SiN and SiH_4 (40 sccm) for Si. The corresponding rate is about 75 nm min^{-1} for SiN and 30 nm min^{-1} for Si. The PECVD deposited film distributed only near the outer surface and cannot go inside due to the low kinetic energy, and thus the film was formed on the CNT papers rather than on the single nanotube. The SiN film is sub-stoichiometric and the atomic N/Si ratio is determined to be 0.8 by using X-ray photoelectron spectroscopy. After film deposition, the samples went through thermal annealing at 450 °C for 20 min in an Ar ambient for improving the film quality.[44] The SiN/Si/SiN composite on the CNT and SS substrates are denoted as the NSN@CNT and NSN@SS anodes respectively. For comparison, a 500 nm Si anode, a 500 nm SiN anode, a 250 nm Si/250 nm SiN composite anode with SiN between the Si and the substrate as the buffer layer (denoted as SN), a 250 nm SiN/250 nm Si composite anode with SiN on the top of the Si film as the clamping layer (denoted as NS) were also prepared by using the same processes mentioned above. Besides, in order to investigate effectiveness of SiN as the clamping or buffer layers, an anode with only 250 nm Si film was also fabricated for comparison. The anodes were prepared on both the CNT (denoted as @CNT) and SS (denoted as @SS) substrates for investigating the effects of the substrates on the anode behaviors.

Material and structural characterization

The thickness of the films was measured by using ellipsometry (Horriba Uvisel). The morphologies of the films were characterized by using scanning electron microscopy (SEM, Zeiss Ultra Plus) and by transmission electron microscopy (TEM, Titan 80-300) combined with energy dispersive X-ray spectroscopy (EDX). The chemical states and composition depth profiles of the films were characterized by using X-ray photoelectron spectroscopy (XPS, PHI Quantera II). The crystalline structure of the films was measured by using X-ray diffraction (XRD, Rigaku Smartlab) and TEM. The compositions of the CNT substrate with and without film coating were measured by using Raman spectroscopy (Horiba T64000). The mechanical properties (including

 © 2021 The Author(s). Published by the Royal Society of Chemistry

Open Access Article. Published on 19 August 2021. Downloaded on 12/6/2025 5:40:57 AM.
This article is licensed under a Creative Commons Attribution-NonCommercial 3.0 Unported Licence.

elastic modulus and hardness) of the CNT substrate before and after cycling were characterized by using nanoindentation (Hysitron TI-750L) with a diamond Berkovich pyramid indenter.

Electrochemical characterization

The anodes were assembled into CR2016-type coin cells with Celgard 2400 as the separator, $LiPF_6$ in ethylene carbonate/dimethyl carbonate (v/v = 1 : 1, from Sigma-Aldrich) as the electrolyte and Li foil as the counter electrode. The electrochemical impedance spectrum (EIS) was measured over the frequency range from 10^5 Hz to 10^{-2} Hz by applying an ac voltage with 5 mV amplitude (CHI 660E). Galvanostatic cycling was carried out between 0.01 V and 3 V *versus* Li/Li^+ (Land CT2001A). After electrochemical cycling, the anodes were took out from the cells and washed in acetonitrile to remove residual electrolyte and then dried in an Ar-filled glove box for 12 hours for physical characterization.

3. Results and discussion

Material characterization

The compositions and chemical states of the films are obtained by XPS combined with curve fittings and also the stacked structures of the composite films are confirmed by using the XPS depth profiling.[8,44] All the films in this work display an amorphous state based on the XRD and TEM characterization according to our previous work.[8,44] Fig. S1† shows the Raman spectrum of the CNT substrate with and without Si film coating. The coated CNT substrate shows lower I_D/I_G ratio than the naked CNT one, indicating fewer defects of the former. High-resolution TEM (HRTEM) and EDX are used to characterize the microstructures near the CNT/Si film interface. As seen in Fig. S2,† CNTs near the surface of the substrate are tightly coated by the deposited film and this is effective to passivate the CNT surficial defects, thus resulting in the lower I_D/I_G ratio.[43] Fig. S3(a) and (b)† shows the SEM morphologies of the fresh CNT substrate, where the CNT texture can be clearly distinguished and each individual CNT intertwines and constructs into an interconnected frame with considerable void space. After depositing 250 nm Si on the CNT substrate, the CNT texture becomes fuzzy but is still distinguishable (as seen in Fig. 2(a)). For comparison, with 500 nm film deposited on the CNT substrate, the CNT texture disappears finally and the surface becomes smooth (as seen in Fig. 2(b)–(f)), corresponding to that the void space near the surface of the CNT substrate is completely filled by the deposited film. This is consistent with the TEM observations shown in Fig. S2.†

Electrochemical characterization

Fig. 3(a) and S4† respectively show the initial charge/discharge voltage profiles of the anodes on the CNT and SS substrates at a low current rate of 0.01C (the current rate of 1C is ~70 μA cm^{-2} for pure CNT, ~350 μA cm^{-2} for Si@CNT, ~140 μA cm^{-2} for SiN@CNT and ~200 μA cm^{-2} for SN@CNT, NS@CNT and NSN@CNT). Compared with the counterpart on the SS substrate, the anode on the CNT substrate displays lower initial coulombic efficiency (ICE) mainly because of larger surface area and more defects of the CNT substrate, which enhance formation of solid-electrolyte interphase (SEI) and irreversible Li^+ trapping during the initial cycling.[25,26,36,41–43] This agrees well with the fact that all the CNT-based anodes exhibit a long voltage plateau at 0.9 V in the initial discharge curve and this plateau also appears in the pure CNT anode, corresponding to the severe SEI formation and irreversible Li^+ trapping of the CNT substrate.[25,26,36,41–43] This plateau disappears in the following cycles (as seen in Fig. 3(b)), suggesting that the SEI formation and irreversible Li^+ trapping mainly occur in the initial cycle. Film coated onto the CNT substrate can passivate the CNT surficial defects (as demonstrated in Fig. S1†) and also reduce reaction between the CNT substrate and the electrolyte, thus helpful to suppress the SEI formation and irreversible Li^+ trapping. Therefore, the film-coated anodes exhibit higher ICE

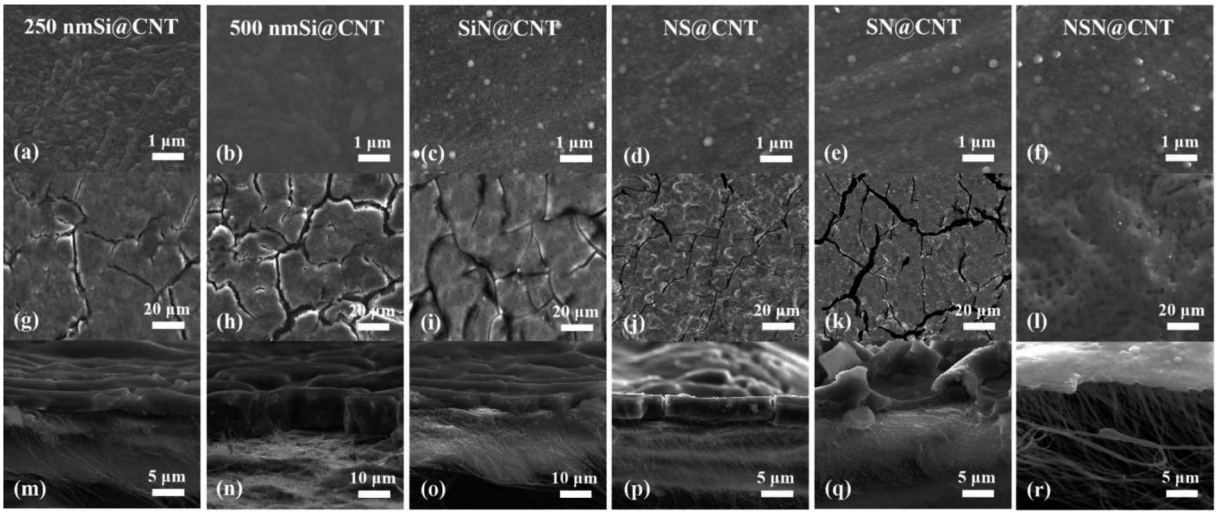

Fig. 2 (a–f) Plan-view SEM images of the CNT-based anodes before cycling. (g–l) Plan-view SEM images and (m–r) cross-sectional SEM images of the CNT-based anodes after 100 cycles.

Open Access Article. Published on 19 August 2021. Downloaded on 12/6/2025 5:40:57 AM.
This article is licensed under a Creative Commons Attribution-NonCommercial 3.0 Unported Licence.

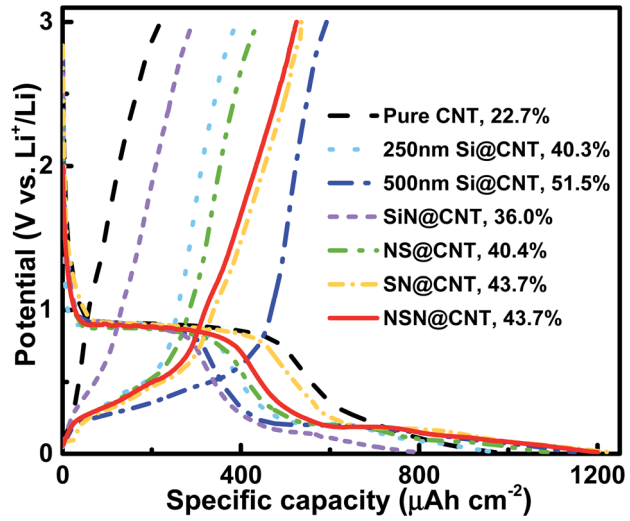

(a)

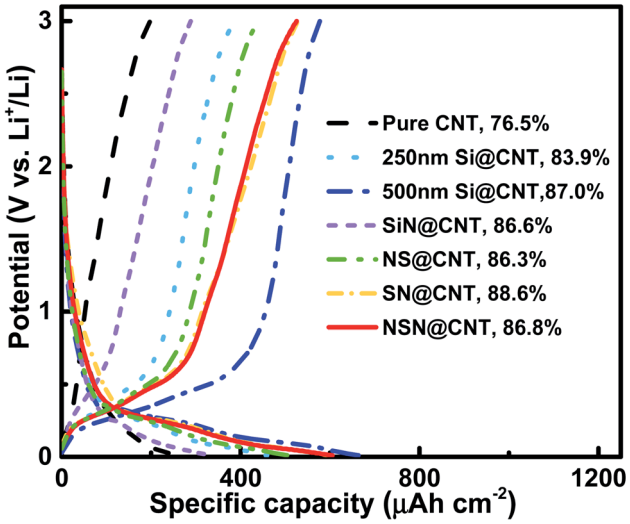

(b)

Fig. 3 Voltage profiles of the pure CNT and CNT-based anodes in the (a) initial cycle and (b) second cycle at 0.01C. The corresponding coulombic efficiency of each anode is also shown. The active film is 500 nm if not otherwise specified.

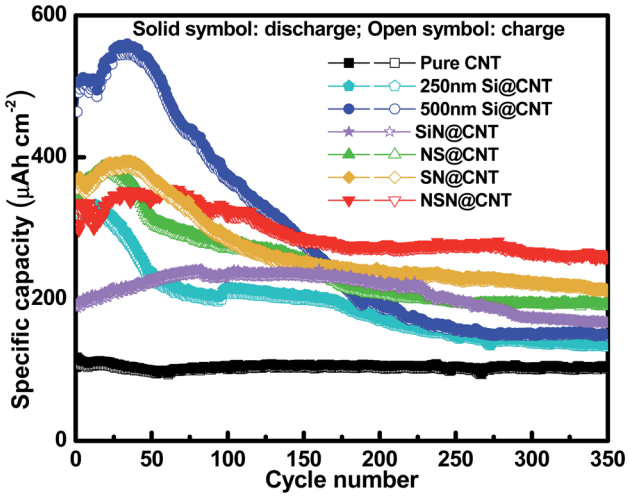

(a)

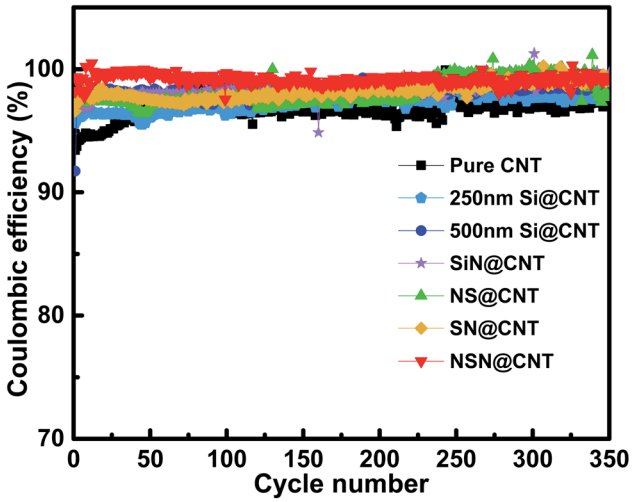

(b)

Fig. 4 (a) Cycling performance of the pure CNT and CNT-based anodes at a current rate of 0.6C. (b) The corresponding coulombic efficiency with cycling. Note that the anodes are activated at a low current density of 0.01C firstly before test.

(~36.0–51.5%) with shorter plateau at 0.9 V than the pure CNT anode (~22.7%). Because the CNT substrate (~10 μm) in this work is much thicker than the coated film (~500 nm), the CNT at the back side of the substrate is hardly covered by the coated film. Therefore, the side reactions of the CNT at the back side of the substrate with the electrolyte also occur in the film-coated anodes and this is consistent with the fact that these anodes also display a short voltage plateau at 0.9 V. Fig. S5† shows the Nyquist plots of the pure CNT and film-coated anodes after the electrochemical activation. Because the film-coated anodes can effectively suppress the SEI formation caused by the reactions of CNT with the electrolyte, they display much higher conductivity than the pure CNT anode. The SEI formation would degrade the conductivity and thus the reaction kinetics;[16,39,47] consequently, for the film-coated anodes, the reaction pathways between the CNT at the back side of the substrate and the electrolyte would be suppressed in the following electrochemical operations. Moreover, for the anodes with the same substrate, the ICE decreases with increasing the SiN composition and the pure SiN anode displays lower ICE than the pure Si one. It has been reported that an irreversible conversion reaction performs between SiN and Li^+ with a formation of elemental Si and inactive lithium compound, followed by a reversible alloying/dealloying reaction of Si with Li^+.[44–46] This irreversible

 © 2021 The Author(s). Published by the Royal Society of Chemistry

Open Access Article. Published on 19 August 2021. Downloaded on 12/6/2025 5:40:57 AM. This article is licensed under a Creative Commons Attribution-NonCommercial 3.0 Unported Licence.

conversion reaction leads to the low ICE of the SiN-containing anodes. Fig. 3(b) shows the charge/discharge voltage profiles of the anodes on the CNT substrate in the 2nd cycle. The Coulombic efficiency (CE) of the CNT-based anodes increase rapidly (≥83.9%) in the 2nd cycle and is usually above 98.0% in the following cycles (as seen in Fig. 4(b)), which is approximate to the CE for the SS-based anodes (as seen in Fig. S6(b)†). For comparison, the CE of the pure CNT anode increases gradually and then maintains a relatively low value (~96.0–98.0%) with cycling due to unstable SEI formation and Li^+ trapping caused by its enlarged surface area contacted with the electrolyte during the lithiation and delithiation processes. The details will be discussed latter. The anode on the CNT substrate exhibits higher areal reversible specific capacity than its counterpart on the SS substrate mainly owing to the electrochemically active nature of the CNT substrate.[41–43]

Fig. 4(a) and S6(a)† respectively show the cycling characteristics of the anodes on the CNT and SS substrates at a current density of 0.6C and the key parameters extracted from the figures are summarized in Table 1. The anode on the CNT substrate displays larger reversible specific capacity and smaller capacity fading (except the SiN anode and the details will be discussed latter) than the counterpart on the SS substrate. This is mainly ascribed to the electrochemically active and elastic properties of the CNT substrate. In addition, unlike those reported Si/CNT configurations with a low Si content (<50 nm) on the CNT substrate which usually present a good cycling stability,[19–23,28–40] the 250 nm Si@CNT anode in this work displays a rapid capacity fading and the retained capacity after 350 cycles is only 42.0% (~135 μA h cm^{-2}). The capacity fading deteriorates with further increasing the Si thickness and only 26.9% of its capacity (~148 μA h cm^{-2}) remains for the 500 nm Si@CNT anode after 350 cycles. The Si@CNT anodes in this work show much worse capacity fading than those reported Si/CNT anode configurations in the literatures mainly due to much higher Si content herein, which causes little void space left to accommodate the Si volume change and thus poor stability. For the 500 nm SiN, SN, NS and NSN@CNT anodes, the capacity retention after 350 cycles is 70.3% (~167 μA h cm^{-2}), 54.5% (~212 μA h cm^{-2}), 50.3% (~190 μA h cm^{-2}) and 73.8% (~259 μA h cm^{-2}), respectively. Both the NS@CNT and SN@CNT anodes have same Si content to the 250 nm Si@CNT one (all including 250 nm Si) but present less severe capacity fading than the latter, indicating the importance of the SiN layer in improving the anode cycling stability. The same phenomenon is also observed for the counterpart anodes on the SS substrate (as seen in Fig. S6(a)†). For the NS@CNT anode, the SiN layer located on the top of the Si layer can serve as a clamping layer to suppress the Si volume change;[13,31,40,47] For the SN@CNT anode, the SiN layer inserted between the Si and CNT substrate can work as a buffer layer to alleviate the stress (caused by the Si volume change) accumulated at the Si/CNT interface.[30,35,44,48] The SiN film has a good cycling stability and considerable specific capacity (as demonstrated in Fig. 4 and S6†) and thus is appropriate as the clamping and buffer layers.[40,44] Generally, regarding a composite consisting of Si and SiN, increasing the Si content (decreasing the SiN content) would improve the specific capacity but degrade the cycling stability; conversely, decreasing the Si content (increasing the SiN content) would degrade the specific capacity but improve the cycling stability. Therefore, the SiN@CNT anode displays better cycling stability than the SN@CNT and NS@CNT ones. The SN@CNT sample shows a little better retained capacity than the NS@CNT one, indicating that the buffer layer plays a more important role in the capacity retention than the clapping layer. Interestingly, the NSN@CNT anode has same compositions to the SN@CNT and NS@CNT ones (all including 250 nm SiN and 250 nm Si) but displays much less capacity fading (as seen in Fig. 4), and the similar advantage can be also found in the group samples with SS as the substrate. Moreover, the NSN@CNT anode even exhibits lower capacity fading than the SiN@CNT anode. The above phenomena demonstrate the effectiveness of the NSN@CNT configuration in improving the anode cycling stability but without sacrificing the specific capacity. Based on the weight of the whole electrode (including the NSN composite and the CNT substrate), the gravimetric specific capacity of the NSN@CNT anode is calculated to be 1023 mA h g^{-1} at 0.01C and 684 mA h g^{-1} at 0.6C, which are higher than that of the commercial graphite anode (~372 mA h g^{-1}). The gravimetric specific capacity of the NSN@CNT anode can be further improved by decreasing the thickness of the CNT substrate (~10 μm herein) since the NSN composite (~2302 mA h g^{-1} for the 0.068 mg NSN composite *vs.* 440 mA h g^{-1} for the 0.189 mg CNT substrate at 0.01C) is the main contributor to the overall specific capacity while the CNT substrate mainly acts as the buffer matrix in this configuration.

Table 1 Performance comparison of the anodes with different composites, different structures and different substrates. For the cycling performance, this table summarizes the reversible capacity and capacity retention of each anode at 0.6C after 350 cycles; for the rate performance, this table shows the recovered capacity rate of each anode as the current rate changes from 0.2C to 24C and then returns to 0.2C

		Samples										
		Si		SiN		SN		NS		NSN		
Performance		@SS	@CNT	@SS	@CNT	@SS	@CNT	@SS	@CNT	@SS	@CNT	Pure CNT
Cycling	Capacity (μA h cm^{-2})	12	148	109	167	51	212	32	190	62	259	103
	Retention	3.1%	26.9%	75.4%	70.3%	25.7%	54.5%	16.5%	50.3%	29.2%	73.8%	93.1%
Rate performance		32.6%	38.3%	98.8%	84.3%	71.4%	79.2%	68.2%	75.3%	94.5%	96.8%	71.9%

Open Access Article. Published on 19 August 2021. Downloaded on 12/6/2025 5:40:57 AM.
This article is licensed under a Creative Commons Attribution-NonCommercial 3.0 Unported Licence.

In order to reveal the mechanism leading to the good cycling stability of the NSN@CNT configuration, the SEM morphologies of the CNT-based anodes after cycling are also shown in Fig. 2(g)–(r). The SEM morphologies of the counterpart anodes on the SS substrate after cycling are shown in Fig. S7.† The SiN/Si/SiN composite film for the NSN@CNT anode is intact and adheres well to the CNT substrate after cycling (as seen in Fig. 2(l)); also, the morphologies of its CNT substrate (as seen in Fig. 2(r)) are very similar to those of the fresh CNT substrate (as seen in Fig. S3(b)†) and each individual CNT in the network can be well distinguished. On the contrary, as shown in Fig. 2(g)–(k), the film for all the other anodes breaks and agglomerates to form island-like cracks with a thickness much larger than the fresh thickness after cycling (this is particularly obvious for the 500 nm Si@CNT anode); moreover, as shown in Fig. 2(m)–(q), the morphologies of their CNT substrate are quite close to those of the cycled CNT anode (as seen in Fig. S3(d)†) and transform into a fully merged network, where each individual CNT and void space in the network become undistinguishable. HRTEM is utilized to gain more details about the morphological evolution of the anodes before and after cycling. As demonstrated in Fig. 5(a) and (c), the cycled NSN@CNT anode displays quite similar CNT morphologies to the fresh CNT anode, where each individual CNT can be clearly defined and presents a smooth and uniform profile. This suggests that the cycling operation has little influence on the morphologies of the CNT substrate and thus the substrate can still maintain excellent mechanical properties and good contact can also be maintained between the CNT and NSN for the cycled NSN@CNT anode. For comparison, as seen in Fig. 5(b), the cycled CNT anode becomes rough and porous and also the CNTs wield together to form a fully merged porous network as previously observed in other nanostructured anodes.[11] The formation of this fully merged porous network has little influence on the cycling stability of the pure CNT anode itself (93.1% of retained capacity after 350 cycles) because of its small volume change (<10%) during the lithiation and delithiation processes;[32] However, compared with the fresh CNT substrate, the fully merged network presents rough and porous profiles, which would enlarge the surface area with the electrolyte and thus result in the relatively low coulombic efficiency of the pure CNT anode as mentioned above. More importantly, since the film coated on the CNT substrate plays the dominant role in the whole specific capacity of the CNT-based anodes as discussed earlier,[2–4,34,41–43] the instability issues of the film caused by the reconstruction of the CNT substrate cannot be ignored. This can be confirmed by the abnormal phenomenon that the SiN@CNT anode displays worse cycling stability than its counterpart on the SS substrate. It is worth pointing out that the main difference of the NSN@CNT anode with the pure CNT and other CNT-based anodes in this work is that the intact SiN/Si/SiN film avoids reaction between the CNT substrate and the electrolyte with cycling; therefore, it is reasonable to conclude that the formation of the fully merged porous CNT network is closely associated with the side reactions of the CNT substrate with the electrolyte, which would enhance kinetics of the Li^+ assisted electrochemically wielding between the neighboring CNTs and pore formation caused by the continual side reactions. Note that the mechanical properties of the CNT substrate are heavily determined by its morphologies.[49] Direct evidence that the cycled CNT anode has much worse mechanical properties than the fresh one is that unlike the fresh one which is flexible and elastic, the cycled CNT anode becomes stiff and brittle. The key mechanical parameters (including elastic modulus and hardness) of the CNT anode before and after cycling can be further quantitatively extracted by using nanoindentation (as seen in Fig. S8†). Nine points are measured for each sample. The average elastic modulus/hardness are 110.6 ± 4.4 MPa/13.4 ± 1.2 MPa for the fresh CNT anode and 442.0 ± 11.9 MPa/112.0 ± 4.8 MPa for the cycled CNT anode. The lower elastic modulus suggests that the corresponding CNT substrate is more competent to act as an elastic buffer matrix for stress relaxation through efficient deformation.[44,50,51] The lower hardness means that the corresponding CNT substrate has higher fracture energy and is more robust against crack.[44,52] The above results suggest that the function of the CNT substrate as the elastic buffer matrix degrades greatly after it transforms into the fully merged network. Based on the above analysis, the robust mechanical strength of the NSN@CNT anode should be mainly ascribed to the synergistic effects as described below: (i) on one hand, both the SiN clamping and buffer layers are beneficial to improve the mechanical stability as discussed earlier and this causes that the NSN@CNT anode has better stability than the Si@CNT ones. In addition, the stress-compensation

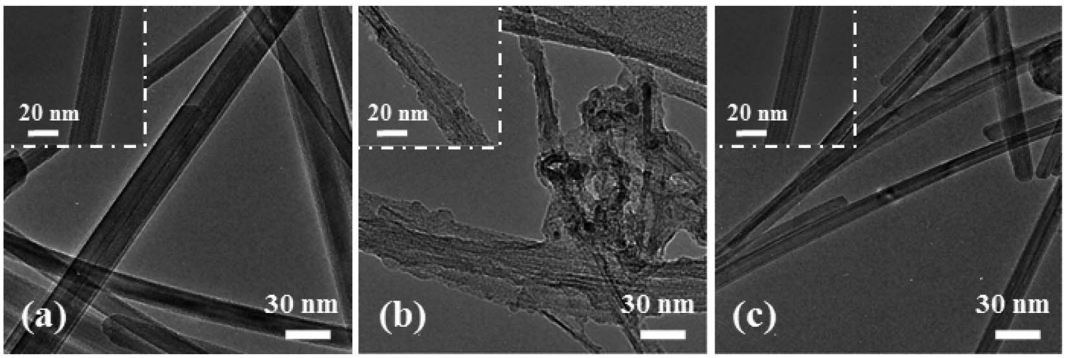

Fig. 5 TEM images of the CNT anode (a) before and (b) after 100 cycles. (c) TEM images of the SiN/Si/SiN@CNT anode after 100 cycles.

 © 2021 The Author(s). Published by the Royal Society of Chemistry

Open Access Article. Published on 19 August 2021. Downloaded on 12/6/2025 5:40:57 AM.
This article is licensed under a Creative Commons Attribution-NonCommercial 3.0 Unported Licence.

phenomenon induced by the symmetrical sandwich-structured configuration is effective to balance and suppress the stress and thus the NSN@CNT anode shows better stability than the SN@CNT and NS@CNT ones.[8,31] Furthermore, the elastic CNT substrate can help release stress. All the above reasons lead to that the SiN/Si/SiN composite film displays a robust mechanical stability with an intact morphology; (ii) on the other hand, the intact composite film blocks reaction of the CNT substrate with the electrolyte and thus the substrate keeps an intact morphology with negligible degradation of its mechanical properties. Consequently, the CNT substrate serves well as the elastic buffer matrix for stress relaxation, thus enhancing the SiN/Si/SiN mechanical stability. The above two sides interrelate and interact with each other to enable the good stability of the NSN@CNT anode. Conversely, for the other anodes, once the film coated on the CNT substrate cracks with cycling, the electrolyte can easily penetrate and contact with the CNT substrate, thus facilitating the formation of the fully merged network with poor mechanical properties. This in turn accelerates the film fracture followed by enhanced formation of the fully merged network iteratively, thus resulting in the poor stability of these anodes.

Fig. 6 and S9† respectively show the rate capacity of the anodes on the CNT and SS substrates at various current rates from 0.2C to 24C and the corresponding key parameters are also summarized in Table 1. Both groups of anodes display same trends, where the pure Si anode and the SiN/Si/SiN anode exhibit the highest and lowest capacity loss with increasing the current rate respectively. The different rate performance of the anodes corresponds to their different mechanical stability. For the NSN@CNT anode, 35.8% (~127 μA h cm^{-2}), 28.4% (~100 μA h cm^{-2}) and 19.4% (~69 μA h cm^{-2}) of its capacity (relative to the initial capacity at 0.2C) can be maintained even at a high current rate of 6C, 12C and 24C respectively. Also, as the current goes back to 0.2C, 96.8% (~342 μA h cm^{-2}) of its capacity can be well recovered with a negligible capacity loss. On the contrary, after going through the same operation, only 38.3% (~202 μA h cm^{-2}), 84.3% (~227 μA h cm^{-2}), 75.3% (~261 μA h cm^{-2}) and 79.2% (~304 μA h cm^{-2}) of the capacity are left for the Si, SiN, NS and SN@CNT anodes respectively. It is noted that even though the NSN@CNT anode has more active materials and longer electron/ion transport pathways than its counterpart on the SS substrate and the pure CNT anode, it shows a comparable (and even better) rate performance compared with the latter anodes, suggesting high reaction kinetics of this unique configuration. In addition, as seen in Table 1, the SiN anode displays better cycling stability and rate performance than the Si, SN and NS ones on both the SS and CNT substrates mainly due to the smaller volume change of the SiN material than the Si one during the electrochemical processes. However, different from those anodes whose performance is improved by using the CNT substrate instead of the SS one (because of the elastic property of the former), the SiN anode on the CNT substrate shows slightly worse performance than its counterpart on the SS substrate. This should be mainly ascribed to the reconstruction of the CNT substrate with cycling, which tends to accelerate collapse of the SiN film and thus degrades the anode performance (as seen in Fig. 2(i), (o) and S7(b)†). The synergistic effects involved in the NSN@CNT anode ensure its best performance among the anodes in this work.

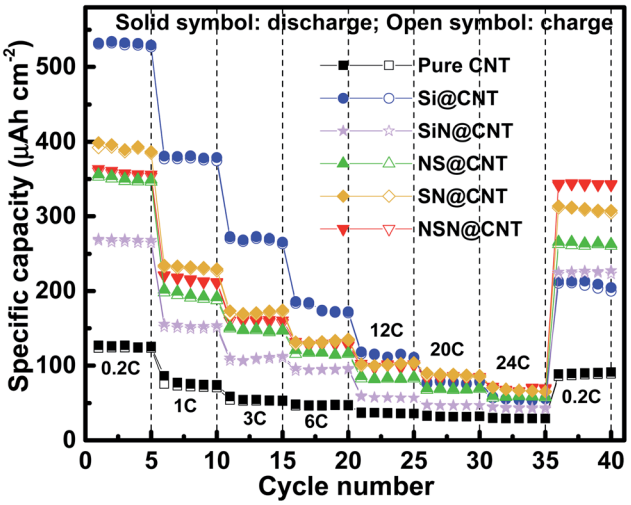

(a)

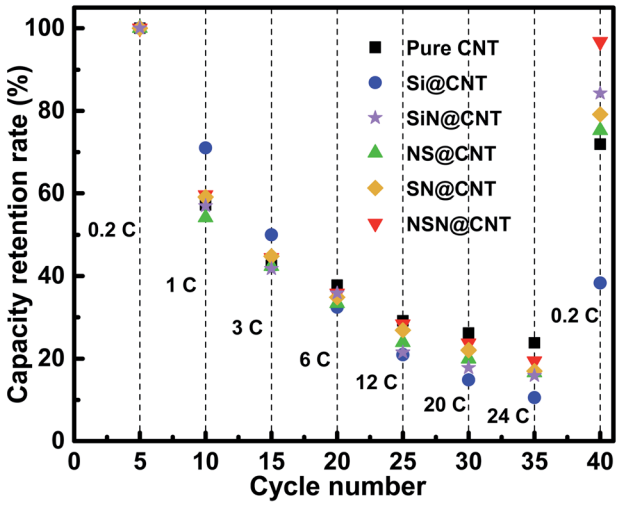

(b)

Fig. 6 (a) Rate performance of the pure CNT and CNT-based anodes. (b) Capacity retention rate of each anode (defined as the ratio of the capacity at a given current rate to the capacity at 0.2C). Note that the anodes are activated at a low current density of 0.01C firstly before test.

4. Conclusion

A freestanding paper-like NSN@CNT anode has been investigated in this work and this unique anode displays high specific capacity (~69 μA h cm^{-2} under the current rate of 24C and the retained capacity is up to 96.8% when the current goes back to 0.2C) even at high current rates without expense of compromising the cycling stability (~259 μA h cm^{-2} under the current

Open Access Article. Published on 19 August 2021. Downloaded on 12/6/2025 5:40:57 AM.
This article is licensed under a Creative Commons Attribution-NonCommercial 3.0 Unported Licence.

rate of 0.6C after 350 cycles, with a capacity retention of 73.8%). By comparison with other anodes with different configurations (including different composites, different structures and different substrates), it is demonstrated that the synergistic effects involved in the unique NSN@CNT configuration are mainly responsible for the high anode performance, which enable that both the SiN/Si/SiN composite film and its CNT substrate retain a robust mechanical stability with cycling and thus good electrochemical performance of the anode. Therefore, the NSN@CNT configuration is promising for high performance lithium-ion battery anodes.

Conflicts of interest

There are no conflicts to declare.

Acknowledgements

This work was supported in part by the National Key R&D Program of China under Grants (No. 2020YFB2007400) and the Natural Outstanding Youth Science Foundation of Jiangsu Province (No. BK20180060), in part by Qing-Lan Project and Six-Talent-Peaks Project of Jiangsu Province.

References

1 T. D. Hatchard and J. R. Dahn, *J. Electrochem. Soc.*, 2004, **151**, A838.
2 W. J. Zhang, *J. Power Sources*, 2011, **196**, 13.
3 B. Liang, Y. P. Liu and Y. H. Xu, *J. Power Sources*, 2014, **267**, 469.
4 H. Kim, E. J. Lee and Y. K. Sun, *Mater. Today*, 2014, **17**, 285.
5 R. Yi, F. Dai, M. L. Gordin, S. R. Chen and D. H. Wang, *Adv. Energy Mater.*, 2013, **3**, 295.
6 M. A. Zhang, T. F. Zhang, Y. F. Ma and Y. S. Chen, *Energy Storage Materials*, 2016, **4**, 1.
7 Y. C. Zhang, Y. You, S. Xin, Y. X. Yin, J. Zhang, P. Wang, X. S. Zheng, F. F. Cao and Y. G. Guo, *Nano Energy*, 2016, **25**, 120.
8 X. D. Huang, F. Zhang, Y. Z. Cao and Q. A. Huang, *J. Electrochem. Soc.*, 2018, **165**, A3397.
9 H. C. Tao, M. A. Huang, L. Z. Fan and X. H. Qu, *Electrochim. Acta*, 2013, **89**, 394.
10 L. Baggetto, D. Danilov and P. H. L. Notten, *Adv. Mater.*, 2011, **23**, 1563.
11 K. Stokes, G. Fynn, H. Geaney, G. Bree and K. M. Ryan, *Nano Lett.*, 2018, **18**, 5569.
12 B. Wang, X. L. Li, T. F. Qiu, B. Luo, J. Ning, J. Li, X. F. Zhang, M. H. Liang and L. J. Zhi, *Nano Lett.*, 2013, **13**, 5578.
13 H. Wu, G. Chan, J. W. Choi, I. Ryu, Y. Yao, M. T. McDowell, S. W. Lee, A. Jackson, Y. Yang, L. B. Hu and Y. Cui, *Nat. Nanotechnol.*, 2012, **7**, 309.
14 Q. B. Zhang, H. X. Chen, L. L. Luo, B. T. Zhao, H. Luo, X. Han, J. W. Wang, C. M. Wang, Y. Yang, T. Zhu and M. L. Liu, *Energy Environ. Sci.*, 2018, **11**, 669.
15 J. H. Cho and S. T. Picraux, *Nano Lett.*, 2013, **13**, 5740.
16 J. Ryu, D. Hong, S. Choi and S. Park, *ACS Nano*, 2016, **10**, 2843.
17 S. H. Kim, D. H. Lee, C. Park and D. W. Kim, *J. Power Sources*, 2018, **395**, 328.
18 Q. Xu, J. Y. Li, J. K. Sun, Y. X. Yin, L. J. Wan and Y. G. Guo, *Adv. Energy Mater.*, 2017, **7**, 6.
19 S. Q. Chen, L. F. Shen, P. A. van Aken, J. Maier and Y. Yu, *Adv. Mater.*, 2017, **29**, 8.
20 J. M. Kim, V. Guccini, K. D. Seong, J. Oh, G. Salazar-Alvarez and Y. Piao, *Carbon*, 2017, **118**, 8.
21 X. Y. Yue, W. Sun, J. Zhang, F. Wang and K. N. Sun, *J. Power Sources*, 2016, **329**, 422.
22 H. Y. Cai, K. Han, H. Jiang, J. W. Wang and H. Liu, *J. Phys. Chem. Solids*, 2017, **109**, 9.
23 B. Liu, P. Soares, C. Checkles, Y. Zhao and G. Yu, *Nano Lett.*, 2013, **13**, 3414.
24 X. H. Wang, L. N. Sun, R. A. Susantyoko, Y. Fan and Q. Zhang, *Nano Energy*, 2014, **8**, 71.
25 K. Yao, J. P. Zheng and Z. Y. Liang, *J. Mater. Res.*, 2018, **33**, 482.
26 S. L. Chou, Y. Zhao, J. Z. Wang, Z. X. Chen, H. K. Liu and S. X. Dou, *J. Phys. Chem. C*, 2010, **114**, 15862.
27 M. W. Forney, R. A. DiLeo, A. Raisanen, M. J. Ganter, J. W. Staub, R. E. Rogers, R. D. Ridgley and B. J. Landi, *J. Power Sources*, 2013, **228**, 270.
28 Q. Z. Xiao, Y. Fan, X. H. Wang, R. A. Susantyoko and Q. Zhang, *Energy Environ. Sci.*, 2014, **7**, 655.
29 L. F. Cui, Y. Yang, C. M. Hsu and Y. Cui, *Nano Lett.*, 2009, **9**, 3370.
30 C. X. Lu, Y. Fan, H. Li, Y. Yang, B. K. Tay, E. Teo and Q. Zhang, *Carbon*, 2013, **63**, 54.
31 J. Y. Liu, N. Li, M. D. Goodman, H. G. Zhang, E. S. Epstein, B. Huang, Z. Pan, J. Kim, J. H. Choi, X. J. Huang, J. H. Liu, K. J. Hsia, S. J. Dillon and P. V. Braun, *ACS Nano*, 2015, **9**, 1985.
32 J. W. Wang, X. H. Liu, K. J. Zhao, A. Palmer, E. Patten, D. Burton, S. X. Mao, Z. G. Suo and J. Y. Huang, *ACS Nano*, 2012, **6**, 9158.
33 K. Evanoff, J. Khan, A. A. Balandin, A. Magasinski, W. J. Ready, T. F. Fuller and G. Yushin, *Adv. Mater.*, 2012, **24**, 533.
34 K. Evanoff, J. Benson, M. Schauer, I. Kovalenko, D. Lashmore, W. J. Ready and G. Yushin, *ACS Nano*, 2012, **6**, 9837.
35 Y. Z. Jiang, H. K. Wang, B. B. Li, Y. Zhang, C. Xie, J. Y. Zhang, G. Chen and C. M. Niu, *Carbon*, 2016, **107**, 600.
36 J. Z. Fu, H. Liu, L. B. Liao, P. Fan, Z. Wang, Y. Y. Wu, Z. W. Zhang, Y. Hai, G. C. Lv, L. F. Mei, H. Y. Hao, J. Xing and J. J. Dong, *Front. Chem.*, 2018, **6**, 9.
37 B. Li, S. B. Yang, S. M. Li, B. Wang and J. H. Liu, *Adv. Energy Mater.*, 2015, **5**, 7.
38 L. F. Cui, L. B. Hu, J. W. Choi and Y. Cui, *ACS Nano*, 2010, **4**, 3671.
39 H. J. Lin, W. Weng, J. Ren, L. B. Qiu, Z. T. Zhang, P. N. Chen, X. L. Chen, J. Deng, Y. G. Wang and H. S. Peng, *Adv. Mater.*, 2014, **26**, 1217.

 © 2021 The Author(s). Published by the Royal Society of Chemistry

Open Access Article. Published on 19 August 2021. Downloaded on 12/6/2025 5:40:57 AM.
This article is licensed under a Creative Commons Attribution-NonCommercial 3.0 Unported Licence.

40 S. J. Kim, M. C. Kim, S. B. Han, G. H. Lee, H. S. Choe, D. H. Kwak, S. Y. Choi, B. G. Son, M. S. Shin and K. W. Park, *Nano Energy*, 2016, **27**, 545.
41 B. J. Landi, R. A. Dileo, C. M. Schauerman, C. D. Cress, M. J. Ganter and R. P. Raffaelle, *J. Nanosci. Nanotechnol.*, 2009, **9**, 3406.
42 S. H. Ng, J. Wang, Z. P. Guo, G. X. Wang and H. K. Liu, *Electrochim. Acta*, 2005, **51**, 23.
43 K. R. Crompton, M. P. Hladky, H. H. Park, S. M. Prokes, C. T. Love and B. J. Landi, *Electrochim. Acta*, 2018, **292**, 628.
44 F. Zhang, Y. Z. Cao, Q. A. Huang and X. D. Huang, *J. Electroanal. Chem.*, 2019, **845**, 119.
45 C. Y. Wu, C. C. Chang and J. G. Duh, *J. Power Sources*, 2016, **325**, 64.
46 X. D. Huang, X. F. Gan, F. Zhang, Q. A. Huang and J. Z. Yang, *Electrochim. Acta*, 2018, **268**, 241.
47 S. Sim, P. Oh, S. Park and J. Cho, *Adv. Mater.*, 2013, **25**, 4498.
48 W. Luo, X. Q. Chen, Y. Xia, M. Chen, L. J. Wang, Q. Q. Wang, W. Li and J. P. Yang, *Adv. Energy Mater.*, 2017, **7**, 28.
49 H. Mukaibo, T. Momma, Y. Shacham-Diamand, T. Osaka and M. Kodaira, *Electrochem. Solid State Lett.*, 2007, **10**, A70.
50 J. P. Maranchi, A. F. Hepp, A. G. Evans, N. T. Nuhfer and P. N. Kumta, *J. Electrochem. Soc.*, 2006, **153**, A1246.
51 Z. Gan, C. Wang and Z. Chen, *Surfaces*, 2018, **1**, 59.
52 R. Furushima, K. Katou, S. Nakao, Z. M. Sun, K. Shimojima, H. Hosokawa and A. Matsumoto, *Int. J. Refract. Met. Hard Mater.*, 2014, **42**, 42.
53 N. Harpak, G. Davidi, Y. Melamed, A. Cohen and F. Patolsky, *Langmuir*, 2020, **36**, 889–896.
54 X. Dai, S. Lei, J. Liu, Z. Shang, S. Zhong and X. Li, *J. Power Sources*, 2021, **498**, 229912.

© 2021 The Author(s). Published by the Royal Society of Chemistry